Room-Temperature Cubic Phase Crystallization and High Stability of Vacuum-Deposited Methylammonium Lead Triiodide Thin Films for High-Efficiency Solar Cells

Francisco Palazon, Daniel Pérez del Rey, Benedikt Dänekamp, Chris Dreessen, Michele Sessolo, Pablo P. Boix* and Henk J. Bolink*

Instituto de Ciencia Molecular, ICMol, Universidad de Valencia, C/ Catedrático J. Beltrán 2, 46980 Paterna, Spain

Methylammonium lead triiodide (MAPI) has emerged as a high-performance photovoltaic material. Common understanding is that at room temperature it adopts a tetragonal phase and it only converts to the perfect cubic phase around 50-60 ºC. Most MAPI films are prepared using a solution-based coating process, yet they can also be obtained by vapor phase deposition methods. Vapor phase processed MAPI films have significantly different characteristics compared to their solvent processed analogous, such as a relatively small crystal grain sizes and short excited state lifetimes. Yet solar cells based on vapor phase processed MAPI films exhibit high power conversion efficiencies. Surprisingly, after detailed characterization we find that our vapor phase processed MAPI films adopt a cubic crystal structure at room temperature that is stable for weeks, even in ambient atmosphere. Furthermore, we demonstrate that by tuning the deposition rates of both precursors during co-deposition it is possible to vary the perovskite phase from cubic to tetragonal at room temperature. Our finding challenges the common belief that MAPI is only stable in tetragonal phase at room temperature. Additionally, these findings can be used to explain the somewhat unexpected high performance of solar cells based on vacuum processed MAPI films with sub 100 nm grain sizes and excited state lifetimes < 100 nanoseconds.

INTRODUCTION

Methylammonium lead triiodide (MAPI) can be considered the archetype alkylammonium lead halide perovskite. It was the first one to be employed in solar cells and remains a reference material used in a variety of research fields today. It is also one of the simplest hybrid perovskites, particularly compared with the mixed cation and anion ones that have emerged more recently[1–3]. Most reports on MAPI films and solar cells use examples prepared by one of the many varieties of solution based processes. [4,5] In virtually all of them, the MAPI films are obtained in the tetragonal crystal structure at room temperature (RT) and they only undergo a phase transition to a cubic structure when the temperature is raised above *ca.* 54 ºC or if pressure is applied.[6–17]

Vapor phase processing of perovskites has also been used for many years, yet due to the requirement of vacuum chambers and control of sublimation it is less widely used in the research community. Nevertheless, there are some specific advantages associated to vapor phase processing, as it avoids (non-benign) solvents, it allows for the precise control of the film thicknesses and it is an intrinsically additive technique which allows for the processing of multiple layers.[18–22]

Although it is not easy to generalize due to the large amount of data on solution processed MAPI films, some differences between solution and vapor phase processed films seem persistent. Particularly, most solution processed films that lead to high performance solar cells have some common features, such as their crystal grain sizes which are in excess of 200 nm and they exhibit an excited state lifetime above 100 ns.[23] In contrast, most vapor phase co-deposited MAPI films have significantly different smaller grain sizes (< 100 nm) ces,[19] and excited state lifetime frequently below 100 ns.[22,24,25] In spite of these differences, quite high performance levels have been obtained for vapor phase processed MAPI containing solar cells, exceeding power conversion efficiencies of 20%.[26]

The question therefore arises whether the differences between films prepared via solution or vapor phase could have their origin in a more profound structural variation.

The crystal structure of the perovskite film has shown to be a critical aspect for material stability and photovoltaic performance. Most of the highest power conversion efficiencies have been achieved by controlling the perovskite lattice structure, which is generally achieved by complex formulations including multiple cations and anions.[1,27] Perovskite crystallization strongly depends on the employed method, and important factors such as the lack of solvents in vapor phase deposition have implications in the film formation. This led us to examine in more detail the crystallinity of our vapor phase deposited MAPI films.

Surprisingly, using high resolution XRD analysis we found that the vacuum-deposited films yielding the highest device performance crystallizes in a cubic perovskite structure at room temperature rather than the expected tetragonal one. This cubic perovskite structure furthermore is very stable over time in both inert and ambient atmospheres. Only by changing the MAI and PbI_2 ratios in the dual source sublimation process the tetragonal phase could be obtained. These results, question the common belief that MAPI at room temperature is only stable in the tetragonal phase. We verify in this work, using a planar solar cell architecture that the cubic MAPI phase leads to very efficient solar cells with high-open circuit voltages and efficiencies above 19 %.

RESULTS

Crystallization of tetragonal and cubic phases.

Thin vapor phase deposited MAPI films (named “standard” in the rest of this work) were prepared by dual-source vacuum sublimation of MAI and PbI_2 (with MAI and PbI_2 deposition rates of 1 Å/s : 0.5 Å/s) following the procedure used to obtain high efficiency solar cells reported previously (and reported in the experimental section for more details).[26,29].

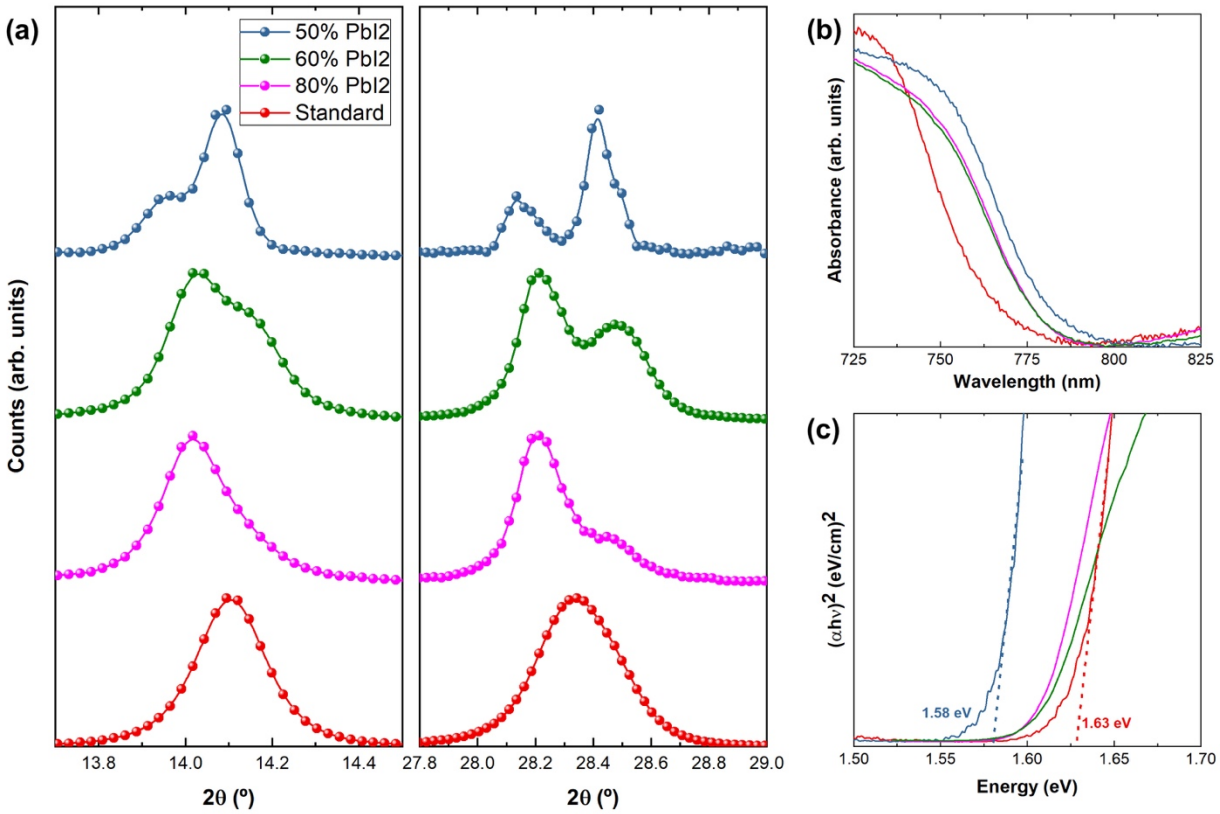

Figure 1. a) High-resolution XRD of MAPI films prepared under standard conditions (bottom, red) and reduced PbI_2 deposition rates. b) Absorption and c) Tauc plot obtained for the same films.

There are several factors that influence the film formation during the sublimation process, such as the substrate temperature, the under-pressure of the chamber during the deposition and the deposition rate of the precursors. During the sublimation process the chamber pressure was maintained in the 10^{-5}–10^{-6} mbar range, and the substrates were kept at room temperature. Modifications in the deposition rate of the precursors resulted in significant structural differences of the obtained perovskite films. High-resolution XRD (Figure 1) shows that MAPI films deposited with a 50% reduction in the PbI_2 rate (setting it at 0.25 Å/s, instead of the standard 0.5 Å/s) crystallize in the tetragonal phase (top diffractogram in blue), as in commonly observed at room temperature. This is clearly visible by the co-existence of two diffraction peaks around 2θ = 14.0º and 14.1º, assigned to the (002) and (110) planes of the tetragonal phase and by the presence oftwo diffraction peaks around

$2\theta = 28.1^{o}$ and 28.4^{o} corresponding to the (004) and (220) planes of the same phase.[9] In films prepared under our standard conditions, in contrast, these signals merge into single reflections at $2\theta = 14.2^{o}$ and 28.5^{o}, which are characteristic of cubic MAPI (bottom diffractogram in red).[9]

These results indicate that tuning the deposition rate of the precursors in the sublimation process enables the modification of the crystalline phase in the thin films. This can be observed from the XRD patterns of the films prepared using intermediate reductions (60 and 80 %) of the standard PbI_2 rate. It should be noted that the modification of the PbI_2 sublimation rate is not accompanied by the appearance of crystalline PbI_2 as evidenced by XRD (see full diffractograms in Figure S1). In solution processed perovskite films the appearance of the cubic phase can be triggered by the use of excess lead precursor in multi-cation and multi-halide perovskites,[30] or by adding a high concentration of hydrohalic acid .[31] In addition several reports mention the co-existence of different crystalline phases, including at RT.[30,32–35] . However, this is the first time that the cubic phase of the pure MAPI perovskite is observed at room temperature.

The morphology of the cubic and tetragonal samples is significantly different as can be seen in Figure S2. Indeed, tetragonal MAPI shows rather large grains of about 1 micron in size as commonly observed in literature. In contrast to this, the cubic phase shows closely-packed smaller grains of about 100 nm. As we will see later, this does not seem to directly influence photovoltaic performance, as we obtain higher PCE with the cubic phase.

The before mentioned different crystal structures also affect the optical properties of the MAPI film. Figure 1 a and b show the absorption spectra of the vapor phase deposited tetragonal and cubic films and the Tauc plots derived from them. Despite some spreading in the reported values for MAPI, there is a general consensus that the phase transition from tetragonal to cubic phases leads to an increase of about 50 meV in the optical bandgap.[7,11] This is in good agreement with both films presented here, as the film demonstrating the tetragonal crystal features shows a narrower bandgap . The wider bandgap of the standard sample corroborates our conclusion that the MAPI films forms in the cubic

phase when deposited using dual-source sublimation under our standard conditions. To further elucidate the energetic levels of both samples, we conducted Air Photoelectron Spectroscopy (APS) measurements (Figure S3). Based on the shift of the valence band observed (5.4 eV for tetragonal MAPI and 5.6 eV for cubic MAPI), and considering the bandgap values obtained from the Tauc plots, we are able to estimate the respective energy diagrams (Figure S3).

In order to obtain further insights on the vacuum deposited MAPI structure, the films were performed *in-situ* temperature-dependent high-resolution XRD analysis from RT to 100 ºC (Figure 2).

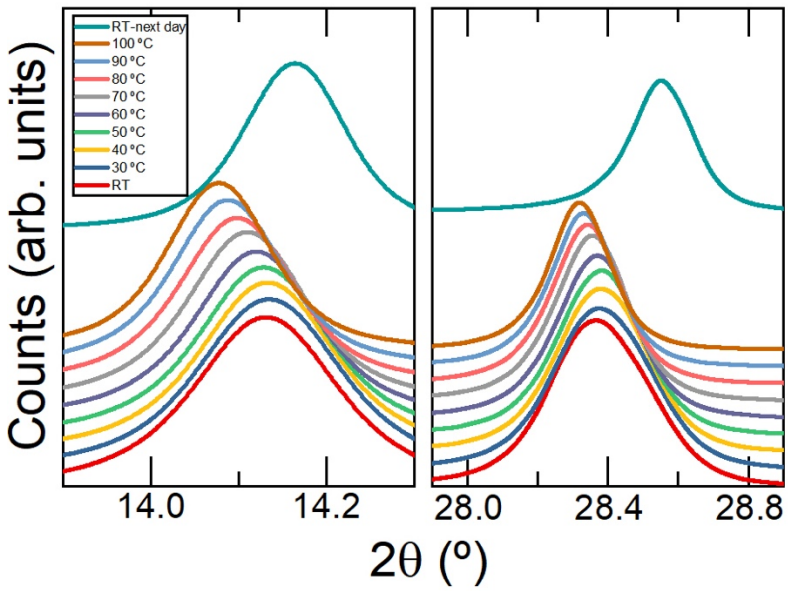

Figure 2. XRD characterization of cubic MAPI film upon in-situ thermal annealing. No phase transition is appreciated.

Figure 2 shows that the peaks assigned to (001) and (002) planes of cubic MAPI shift towards lower angle (higher interatomic distance) as expected from thermal expansion of the lattice (see Figure S4 for a quantitative assessment of the shift).[9] Furthermore, peaks become narrower upon heating which could be linked to grain growth or sintering. Indeed, by applying Scherrer's equation, we observe a steady increase of the typical crystallite size (i.e., grain size) from around 30 nm at RT to 45 nm at 100 ºC (see Figure S4). Despite these gradual changes which are rather common for all types of polycrystalline materials, no phase transition is appreciated within this temperature range, in contrast

to solution processed MAPI thin films and single crystals,[10] which undergo a tetragonal to cubic phase transition upon heating. This is a further confirmation that the as-deposited MAPI obtained by vacuum co-deposition is in its cubic phase at the beginning of the experiment at RT, and discards possible phase retention effects observed in solution processed MAPI.[36] The analysis of the film after cooling down to RT one day after annealing (Figure 2, top diffractogram) again shows the cubic structure of the sample, with a slight shift to higher angles (lower interatomic distances). This suggests a minor shrinkage of the lattice, but there are no indications of a cubic to tetragonal phase transition. In contrast, when the tetragonal MAPI obtained with 0.5 PbI_2 rate film is heated above 54 ºC, it undergoes the expected phase transition into cubic MAPI (see Figure S5), as frequently reported by others.[7–9,16]

Stability.

Hybrid perovskite thin films are known to be prone to degradation when exposed to external agents such as oxygen, water (moisture), heat or other.[37,38] Here, we have tested the stability of cubic MAPI thin films in different atmospheres (see Figures 3 and 4).

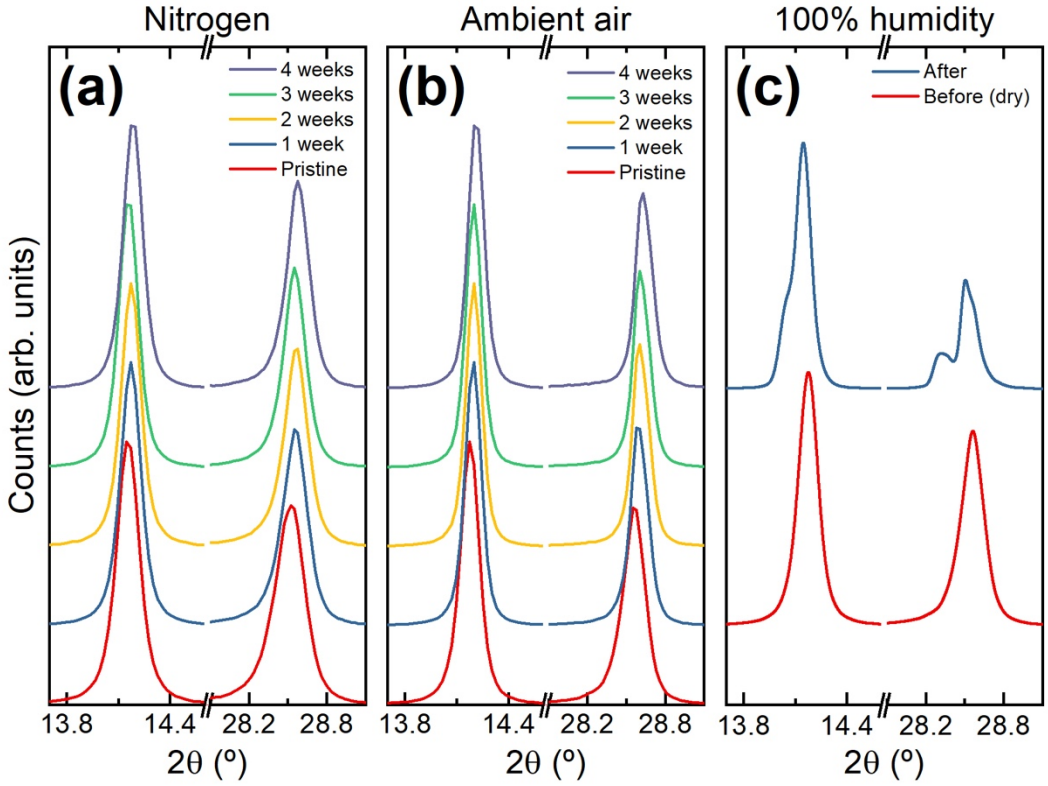

Figure 3. XRD of samples aged under different conditions: (a) samples are kept in a nitrogen-filled glove box for several weeks, (b) samples are kept in air on a shelf, with a varying relative humidity for several weeks (c) samples are exposed to a saturated moisture environment for ca. 1 min by placing them in a closed petri dish with liquid water (liquid not in direct contact with samples).

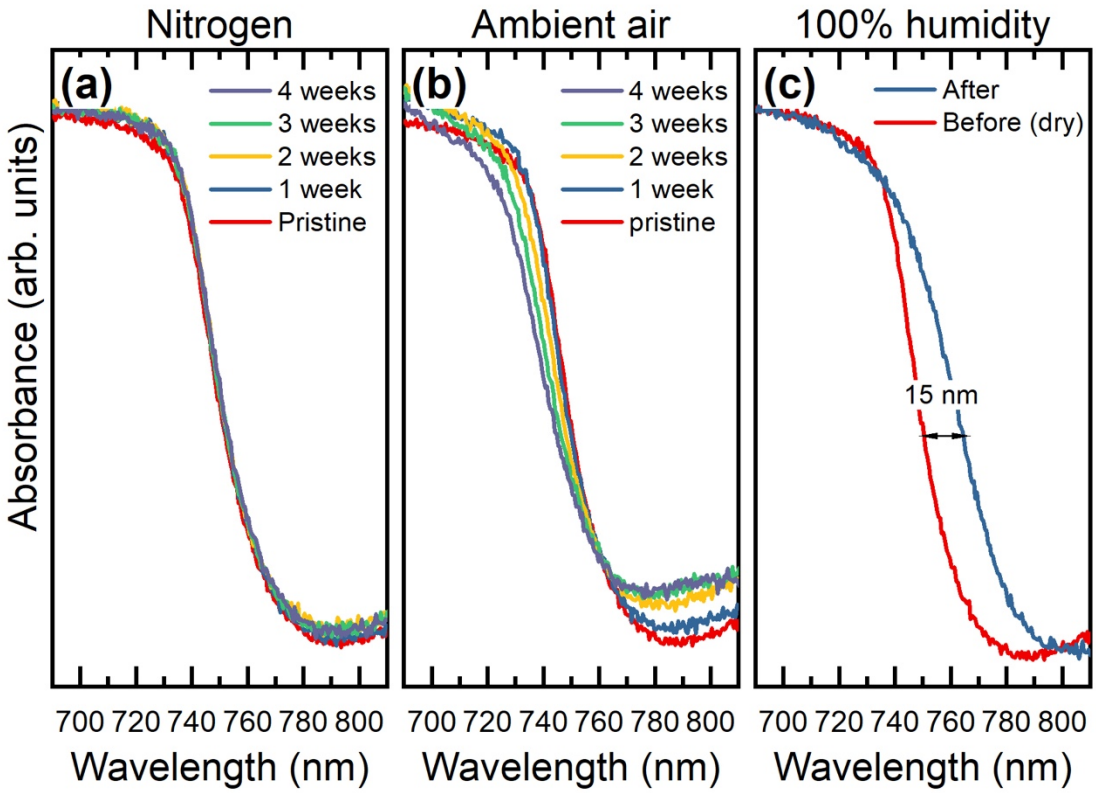

Figure 4. Absorbance spectra of samples aged under different conditions: (a) samples are kept in a nitrogen-filled glove box for several weeks, (b) samples are kept in air on a shelf, with a varying relative humidity for several weeks (c) samples are exposed to a saturated moisture environment for ca. 1 min by placing them in a closed petri dish with liquid water (liquid not in direct contact with samples).

When the film is kept under nitrogen (Figure 3a and 4a) no significant changes can be observed in the timespan of 4 weeks. More strikingly, even when the films are kept in air without humidity control (40-60% relative humidity, 22-25 ºC), the XRD signal remains very similar in the same timespan (Figure 3b) and consistent with cubic MAPI. The full diffractograms (Figure S6) show only a moderate increase in PbI_2 content. We also note that the absorption onset (Figure 4b) becomes slightly less marked over time, which may point to some extent of degradation, although no clear shift is observed. This demonstrates an exceptionally high stability of cubic MAPI thin films in air. Eventually, it is only when the sample is placed in a saturated moisture environment (Figures 3c and

4c) that a clear transition into the tetragonal phase is observed. In contrast to this, tetragonal MAPI prepared with 50% of the standard PbI2 rate is rapidly degraded in air (see Figure S7).

Solar cells

In order to evaluate the implications of our findings in the actual performance of solar cells, we implemented these cubic MAPI thin films in single junction n-i-p photovoltaic devices with the following device architecture: ITO / TiO_2 / C_{60} / MAPI / TaTm / TaTm:F_6-TCNNQ / Au. Details on the fabrication of these devices are reported elsewhere.[26] Figure 5a shows the derivative of the external quantum efficiency (EQE) spectrum, which allows to precisely determine the bandgap of the semiconductor.[39] Here, we find a value of 1.63 eV, fully consistent with the value obtained by optical absorption (Figure 1). It is worth noting that upon heating (see Figure S4), this value increases marginally. Such a monotonic increase in bandgap is reported in literature for the same crystalline phase, suggesting to be related with thermal expansion of the lattice rather than a phase transition.[7] Therefore, this confirms that the vacuum-deposited perovskite solar cell retains the cubic phase which determines the performance of the devices due to a more symmetric absorber, and it rules out possible ferroelectric contributions to the photovoltaic performance.[40] In detail, Figure 5b depicts a representative I-V curve of the same device without significant hysteresis. The results show a power conversion efficiency of 19.7 % with an open-circuit voltage of 1.16 V, among the highest voltages for MAPI solar cells reported to date.[22,26,41] The full EQE with the corresponding integrated current at AM1.5G, statistical photovoltaic parameters dispersion and maximum power point tracking are represented in Figures S9, S10 and S11. It is worth noting that when vacuum-deposited tetragonal MAPI is used instead, considerably worse photovoltaic performances are obtained (see Figure S12).

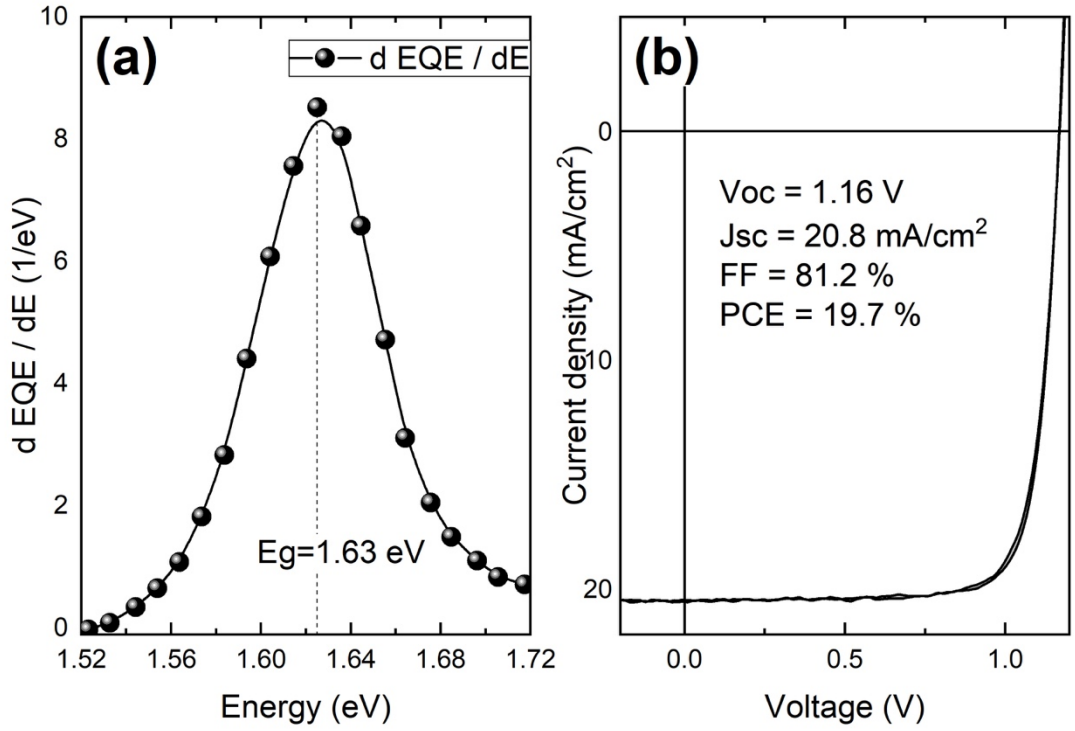

Figure 5. Derivative of EQE (left) and J-V curves in forward and reverse directions (right) of a representative solar cell made with cubic MAPI.

Conclusion

In summary, we have shown that the cubic phase of MAPI can be stable in thin films at room temperature. This is possible by tuning the deposition rates in a dual-source vapor phase process. Furthermore, the cubic MAPI thin films are found to be highly stable not only under inert atmosphere but also in air. Solar cells made thereof exhibit high open-circuit voltages and overall power conversion efficiency, ruling out possible ferroelectric contributions.

Methods

Chemicals. Photolithographically patterned ITO coated glass substrates were purchased from Naranjo Substrates. N4,N4,N4″,N4″-tetra([1,1′-biphenyl]-4-yl)-[1,1′:4′,1″-terphenyl]-4,4″-diamine (TaTm) and F_6-TCNNQ were provided from Novaled GmbH. TiO_2 nanoparticle suspensions were

prepared in IMEC following the preparation procedure explained in reference 26. Fullerene (C_{60}) was purchased from sigma Aldrich. PbI_2 was purchased from Tokyo Chemical Industry CO (TCI) and CH3NH3I (MAI) was purchased from Lumtec.

Vacuum deposition. ITO prepatterned substrates were cleaned following a standard procedure: first they are cleaned with soap, water, deionized water and isopropanol in a sonication bath, followed by a 20 min UV treatment. The TiO_2 dispersion was deposited in air by spin-coating at 3000 rpm for 30 s and annealed at 100 °C for 30 min, leading to a 50−80 nm thick compact layer. Then, the samples were transferred to a vacuum chamber integrated into a nitrogen-filled glovebox (H_2O and O2 < 0.1 ppm) and evacuated to a pressure of 10−6 mbar. The vacuum chamber is equipped with six temperature-controlled evaporation sources (Creaphys) fitted with ceramic crucibles. The sources were directed upward with an angle of approximately 90° with respect to the bottom of the evaporator. The substrate holder to evaporation sources distance is approximately 20 cm. Three quartz crystal microbalance (QCM) sensors are used, two monitoring the deposition rate of each evaporation source and a third one close to the substrate holder monitoring the total deposition rate. For thickness calibration, we individually sublimed the charge transport materials. A calibration factor was obtained by comparing the thickness inferred from the QCM sensors with that measured with a mechanical profilometer (Ambios XP1). Then, the materials were sublimed at temperatures ranging from 160 ºC to >300 ºC, and the evaporation rate was controlled by separate QCM sensors obtaining precisely the deposited thickness. In general, the deposition rate for TaTm and C_{60} was 0.5 Å s−1 and 0.8 Å s−1 for the TaTm/F_6-TCNNQ coevaporation. TaTm doped layer was obtained by coevaporation of TaTm and the dopant F_6-TCNNQ controlling in different sensor the deposition rate of each material, following the procedure described in reference 29 .For the perovskite deposition, MAI and PbI_2 were also coevaporated by measuring the deposition rate of each material in a different sensor and obtaining the total perovskite thickness in a third one, leading to 590 nm thick perovskite. Au was evaporated in a second vacuum chamber with the same working principle as the first one previously described, using aluminium boats as heating sources.

X-ray diffraction. X-ray diffraction was measured with a Panalytical Empyrean diffractometer equipped with CuKα anode operated at 45 kV and 30 mA and a Pixcel 1D detector in scanning line mode. Single scans were acquired in the 2Θ = 10º to 50º range in Bragg-Brentano geometry in air. Anti-scatter slits of 1/16º and step-sizes of 0.025º were used for high-resolution diffractograms. Data analysis was performed with HighScore Plus software. In-situ annealing studies were performed by placing the samples onto a home-made aluminum heating stage (open, in air).

Optical characterization. Absorbance was measured with a High Power UV-VIS fiber light source, integrated sphere and Avantes Starline AVASpec-2048L spectrometer.

J-V curves. For the solar cell characterization, the external quantum efficiency (EQE) was estimated using the cell response at different wavelengths. The cell was placed in an evacuated (1 mbar) INSTEC temperature stage and illuminated by a Quartz-Tungsten-Halogen lamp (Newport Apex 2-QTH) through a monochromator (Newport CS130-USB-3-MC) and a chopper at 235 Hz. The device current was measured as a function of energy in 0.01 eV steps using a lock-in amplifier (Stanford Research Systems SR830). The system was calibrated and the solar spectrum mismatch is corrected using a calibrated Silicon reference cell (MiniSun simulator by ECN, The Netherlands)

The J−V characteristics were obtained using a WaveLabs Sinus 50 solar simulator with spectral response matching AM1.5G illumination. Before each measurement, the exact light intensity was determined using a calibrated Si reference diode equipped with an infrared cutoff filter (KG-3, Schott). The J−V curves were recorded without device preconditioning between −0.2 and 1.2 V (forward) and between 1.2 and −0.2 V (reverse) with 0.01 V steps, integrating the signal for 20 ms after a 10 ms delay. This corresponds to a speed of about 0.3 V s−1. The layout used to test the solar cells has four equal areas (0.0653 cm^2, defined as the overlap between the ITO and the top metal contact) and measured through a shadow mask with 0.04 cm^2 aperture.

Acknowledgements

The research leading to these results has received funding from the European Union Programme for Research and Innovation Horizon 2020 (2014-2020) under the Marie Skłodowska-Curie Grant Agreement PerovSAMs No. 747599, and project INFORM (grant 675867), the Spanish Ministry of Economy and Competitiveness (MINECO) via the Unidad de Excelencia María de Maeztu MDM-2015-0538, MAT2017-88821-R, MAT2017-88905-P and PCIN-2015-255, and the Generalitat Valenciana (Prometeo/2016/135). H. J. B. acknowledges the support of ERA NET PCIN-2017-014. M. S. and P.P.B. thank the MINECO for their respective post-doctoral RyC contracts. PPB acknowledges the financial support from the Conselleria d'Educació, Investigació, Cultura i Esport Valenciana (SEJI2017/2017/012).

Author contributions

P.P.B., H.J.B., M.S., and F.P. designed the experiments. D.P. and B.D. deposited the thin films. D.P. made the solar cells and measured J-V curves. F.P. measured and analyzed XRD. C.D. measured and analyzed EQE. All authors contributed to writing the article. P.P.B., H.J.B. supervised the project.

Additional information

Supplementary information with additional XRD, APS, and device performance is available.

.

Competing interests

The authors declare no competing interests.

References

(1) Saliba, M.; Matsui, T.; Seo, J.-Y.; Domanski, K.; Correa-Baena, J.-P.; Nazeeruddin, M. K.; Zakeeruddin, S. M.; Tress, W.; Abate, A.; Hagfeldt, A.; et al. Cesium-Containing Triple Cation Perovskite Solar Cells: Improved Stability, Reproducibility and High Efficiency. *Energy Environ. Sci.* **2016**, *9* (6), 1989–1997.

(2) Saliba, M.; Matsui, T.; Domanski, K.; Seo, J.-Y.; Ummadisingu, A.; Zakeeruddin, S. M.; Correa-Baena, J.-P.; Tress, W. R.; Abate, A.; Hagfeldt, A.; et al. Incorporation of Rubidium Cations into Perovskite Solar Cells Improves Photovoltaic Performance. *Science (80-.).* **2016**, *354* (6309), 206–209.

(3) Yang, W. S.; Park, B.-W.; Jung, E. H.; Jeon, N. J.; Kim, Y. C.; Lee, D. U.; Shin, S. S.; Seo, J.; Kim, E. K.; Noh, J. H.; et al. Iodide Management in Formamidinium-Lead-Halide–based Perovskite Layers for Efficient Solar Cells. *Science (80-.).* **2017**, *356* (6345), 1376–1379.

(4) Cui, P.; Wei, D.; Ji, J.; Huang, H.; Jia, E.; Dou, S.; Wang, T.; Wang, W.; Li, M. Planar P–n Homojunction Perovskite Solar Cells with Efficiency Exceeding 21.3%. *Nat. Energy* **2019**, 1.

(5) Correa-Baena, J.-P.; Abate, A.; Saliba, M.; Tress, W.; Jesper Jacobsson, T.; Grätzel, M.; Hagfeldt, A. The Rapid Evolution of Highly Efficient Perovskite Solar Cells. *Energy Environ. Sci.* **2017**, *10* (3), 710–727.

(6) Birkhold, S. T.; Hu, H.; Höger, P. T.; Wong, K. K.; Rieder, P.; Baumann, A.; Schmidt-Mende, L. Mechanism and Impact of Cation Polarization in Methylammonium Lead Iodide. *J. Phys. Chem. C* **2018**.

(7) Quarti, C.; Mosconi, E.; Ball, J. M.; D'Innocenzo, V.; Tao, C.; Pathak, S.; Snaith, H. J.; Petrozza, A.; De Angelis, F. Structural and Optical Properties of Methylammonium Lead Iodide across the Tetragonal to Cubic Phase Transition: Implications for Perovskite Solar Cells. *Energy Environ. Sci.* **2016**, *9* (1), 155–163.

(8) Whitfield, P. S.; Herron, N.; Guise, W. E.; Page, K.; Cheng, Y. Q.; Milas, I.; Crawford, M. K. Structures, Phase Transitions and Tricritical Behavior of the Hybrid Perovskite Methyl Ammonium Lead Iodide. *Sci. Rep.* **2016**, *6* (June), 1–16.

(9) Jacobsson, T. J.; Schwan, L. J.; Ottosson, M.; Hagfeldt, A.; Edvinsson, T. Determination of Thermal Expansion Coefficients and Locating the Temperature-Induced Phase Transition in Methylammonium Lead Perovskites Using X-Ray Diffraction. *Inorg. Chem.* **2015**, *54* (22), 10678–10685.

(10) Baikie, T.; Fang, Y.; Kadro, J. M.; Schreyer, M.; Wei, F.; Mhaisalkar, S. G.; Graetzel, M.; White, T. J. Synthesis and Crystal Chemistry of the Hybrid Perovskite (CH3NH3)PbI3 for Solid-State Sensitised Solar Cell Applications. *J. Mater. Chem. A* **2013**, *1* (18), 5628.

(11) Szafrański, M.; Katrusiak, A. Mechanism of Pressure-Induced Phase Transitions, Amorphization, and Absorption-Edge Shift in Photovoltaic Methylammonium Lead Iodide. *J. Phys. Chem. Lett.* **2016**, *7* (17), 3458–3466.

(12) Mashiyama, H.; Kurihara, Y. Disordered Cubic Perovskite Structure of CH3NH3PbX3 (X=Cl, Br, I). *J. Korean Phys. Soc.* **1998**, *32*, 156–158.

(13) Kawamura, Y.; Mashiyama, H.; Hasebe, K. Structural Study on Cubic–Tetragonal Transition of $CH_3NH_3PbI_3$. *J. Phys. Soc. Japan* **2002**, *71* (7), 1694–1697.

(14) Weber, D. CH 3 NH 3 PbX 3 , Ein Pb(II)-System Mit Kubischer Perowskitstruktur. **2015**, *1445* (August 1978), 1443–1445.

(15) Poglitsch, A.; Weber, D. Dynamic Disorder in Methylammoniumtrihalogenoplumbates (II) Observed by Millimeter-Wave Spectroscopy. *J. Chem. Phys.* **1987**, *87*, 6373.

(16) Weller, M. T.; Weber, O. J.; Henry, P. F.; Di Pumpo, A. M.; Hansen, T. C. Complete Structure and Cation Orientation in the Perovskite Photovoltaic Methylammonium Lead Iodide between 100 and 352 K. *Chem. Commun.* **2015**, *51* (20), 4180–4183.

(17) Baikie, T.; Barrow, N. S.; Fang, Y.; Keenan, P. J.; Slater, P. R.; Piltz, R. O.; Gutmann, M.; Mhaisalkar, S. G.; White, T. J. A Combined Single Crystal Neutron/X-Ray Diffraction and Solid-State Nuclear Magnetic Resonance Study of the Hybrid Perovskites CH $_3$ NH $_3$ PbX $_3$ (X = I, Br and Cl). *J. Mater. Chem. A* **2015**, *3* (17), 9298–9307.

(18) Olthof, S.; Meerholz, K. Substrate-Dependent Electronic Structure and Film Formation of MAPbI 3 Perovskites. *Sci. Rep.* **2017**, *7* (December 2016), 1–10.

(19) Ávila, J.; Momblona, C.; Boix, P. P.; Sessolo, M.; Bolink, H. J. Vapor-Deposited Perovskites: The Route to High-Performance Solar Cell Production? *Joule* **2017**, *1* (3), 431–442.

(20) Hwang, B.; Lee, J.-S. A Strategy to Design High-Density Nanoscale Devices Utilizing Vapor Deposition of Metal Halide Perovskite Materials. *Adv. Mater.* **2017**, *1701048*, 1701048.

(21) Ono, L. K.; Wang, S.; Kato, Y.; Raga, S. R.; Qi, Y. Semi-Transparent Perovskite Films with Centimeter-Scale Superior Uniformity by the Hybrid Deposition Method. *Energy Environ. Sci.* **2014**.

(22) Ávila, J.; Momblona, C.; Boix, P.; Sessolo, M.; Anaya, M.; Lozano, G.; Vandewal, K.; Míguez, H.; Bolink, H. J. High Voltage Vacuum-Deposited CH 3 NH 3 PbI 3 –CH 3 NH 3 PbI 3 Tandem Solar Cells. *Energy Environ. Sci.* **2018**.

(23) Nie, W.; Tsai, H.; Asadpour, R.; Neukirch, A. J.; Gupta, G.; Crochet, J. J.; Chhowalla, M.; Tretiak, S.; Alam, M. a; Wang, H. High-Efficiency Solution-Processed Perovskite Solar Cells with Millimeter-Scale Grains. *Science (80-.).* **2015**, *347* (6221), 522–525.

(24) Nagiri, R. C. R.; Meredith, P.; Armin, A.; Lin, Q.; Burn, P. L. Electro-Optics of Perovskite Solar Cells. *Nat. Photonics* **2014**, *9* (2), 106–112.

(25) Anaya, M.; Correa-Baena, J. P.; Lozano, G.; Saliba, M.; Anguita, P.; Roose, B.; Abate, A.; Steiner, U.; Grätzel, M.; Calvo, M. E.; et al. Optical Analysis of CH3NH3Sn:XPb1- XI3 Absorbers: A Roadmap for Perovskite-on-Perovskite Tandem Solar Cells. *J. Mater. Chem. A* **2016**, *4* (29), 11214–11221.

(26) Pérez-Del-Rey, D.; Boix, P. P.; Sessolo, M.; Hadipour, A.; Bolink, H. J. Interfacial Modification for High-Efficiency Vapor-Phase-Deposited Perovskite Solar Cells Based on a Metal Oxide Buffer Layer. *J. Phys. Chem. Lett.* **2018**, *9* (5), 1041–1046.

(27) Saliba, M.; Matsui, T.; Domanski, K.; Seo, J.; Ummadisingu, A.; Zakeeruddin, S. M.; Correa-Baena, J. P.; Tress, W. R.; Abate, A.; Hagfeldt, A.; et al. Incorporation of Rubidium Cations into Perovskite Solar Cells Improves Photovoltaic Performance Incorporation of Rubidium Cations into Perovskite Solar Cells Improves Photovoltaic Performance. *Science (80-.).* **2016**, *5557* (September), 1–8.

(28) King, A. H. Our Elemental Footprint. *Nat. Mater.* **2019**.

(29) Momblona, C.; Gil-Escrig, L. L.; Bandiello, E.; Sessolo, M.; Hutter, E. M.; Lederer, K.; Blochwitz-Nimoth, J. B.-N.; Bolink, H. J.; Sessolo, M.; Lederer, K.; et al. Efficient Vacuum Deposited P-i-n and n-i-p Perovskite Solar Cells Employing Doped Charge Transport Layers.

Energy Environ. Sci. **2016**, *9* (11), 3456–3463.

(30) Park, B. wook; Kedem, N.; Kulbak, M.; Lee, D. Y.; Yang, W. S.; Jeon, N. J.; Seo, J.; Kim, G.; Kim, K. J.; Shin, T. J.; et al. Understanding How Excess Lead Iodide Precursor Improves Halide Perovskite Solar Cell Performance. *Nat. Commun.* **2018**, *9* (1), 1–8.

(31) Myae, C.; Soe, M.; Stoumpos, C. C.; Harutyunyan, B.; Manley, E. F.; Chen, L. X.; Bedzyk, M. J.; Marks, T. J. Room Temperature Phase Transition in Methylammonium Lead Iodide Perovskite Thin Films Induced by Hydrohalic Acid Additives. **2016**, 2656–2665.

(32) Kim, T. W.; Uchida, S.; Matsushita, T.; Cojocaru, L.; Jono, R.; Kimura, K.; Matsubara, D.; Shirai, M.; Ito, K.; Matsumoto, H.; et al. Self-Organized Superlattice and Phase Coexistence inside Thin Film Organometal Halide Perovskite. *Adv. Mater.* **2018**, *30* (8), 1–8.

(33) Song, Z.; Watthage, S. C.; Phillips, A. B.; Tompkins, B. L.; Ellingson, R. J.; Heben, M. J. Impact of Processing Temperature and Composition on the Formation of Methylammonium Lead Iodide Perovskites. *Chem. Mater.* **2015**, *27* (13), 4612–4619.

(34) Zhu, T.; Ertekin, E. Mixed Phononic and Non-Phononic Transport in Hybrid Lead Halide Perovskites: Glass-Crystal Duality, Dynami- Cal Disorder, and Anharmonicity. *Energy Environ. Sci.* **2018**.

(35) Yaghoobi Nia, N.; Zendehdel, M.; Cinà, L.; Matteocci, F.; Di Carlo, A. A Crystal Engineering Approach for Scalable Perovskite Solar Cells and Module Fabrication: A Full out of Glove Box Procedure. *J. Mater. Chem. A* **2018**, *6* (2), 659–671.

(36) Osherov, A.; Hutter, E. M.; Galkowski, K.; Brenes, R.; Maude, D. K.; Nicholas, R. J.; Plochocka, P.; Bulović, V.; Savenije, T. J.; Stranks, S. D. The Impact of Phase Retention on the Structural and Optoelectronic Properties of Metal Halide Perovskites. *Adv. Mater.* **2016**, *28* (48), 10757–10763.

(37) Manser, J. S.; Saidaminov, M. I.; Christians, J. A.; Bakr, O. M.; Kamat, P. V. Making and Breaking of Lead Halide Perovskites. *Acc. Chem. Res.* **2016**, *49* (2), 330–338.

(38) Palazon, F.; Pérez-del-Rey, D.; Marras, S.; Prato, M.; Sessolo, M.; Bolink, H. J.; Manna, L. Coating Evaporated MAPI Thin Films with Organic Molecules: Improved Stability at High Temperature and Implementation in High-Efficiency Solar Cells. *ACS Energy Lett.* **2018**, 835–839.

(39) Rau, U.; Blank, B.; Müller, T. C. M.; Kirchartz, T. Efficiency Potential of Photovoltaic Materials and Devices Unveiled by Detailed-Balance Analysis. *Phys. Rev. Appl.* **2017**, *7* (4), 1–9.

(40) Oron, D.; Kaslasi, H.; Lubomirsky, I.; Meirzadeh, E.; Cahen, D.; Bar-Elli, O.; Ehre, D.; Peleg, Y.; Hodes, G.; Rakita, Y. Tetragonal CH 3 NH 3 PbI 3 Is Ferroelectric . *Proc. Natl. Acad. Sci.* **2017**, *114* (28), E5504–E5512.

(41) Wolff, C. M.; Zu, F.; Paulke, A.; Toro, L. P.; Koch, N.; Neher, D. Reduced Interface-Mediated Recombination for High Open-Circuit Voltages in CH 3 NH 3 PbI 3 Solar Cells. *Adv. Mater.* **2017**, *29* (28), 1700159.